Monthly Notices of the ROYAL ASTRONOMICAL SOCIETY

MNRAS **548,** 1–15 (2026) https://doi.org/10.1093/mnras/stag447
Advance Access publication 2026 March 5

Detection of C_3 in Titan with VLT-ESPRESSO

R. Rianço-Silva ,[1,2,3]★ P. Machado,[2,3] P. Rannou,[4] J. Martins,[5] A. E. Lynas-Gray[1,6,7] and G. Tinetti[8]

[1]*Department of Physics and Astronomy, University College London, Gower Street, WC1E 6BT London, UK*
[2]*Instituto de Astrofísica e Ciências do Espaço, Universidade de Lisboa, OAL, Edifício Leste, Tapada da Ajuda, P-1349-018 Lisbon, Portugal*
[3]*Departamento de Física, Faculdade de Ciências, Universidade de Lisboa, Edifício C8, Campo Grande, P-1749-016 Lisbon, Portugal*
[4]*Université de Reims Champagne-Ardenne 51687, Reims, France*
[5]*Instituto de Astrofísica e Ciências do Espaço, Universidade do Porto, CAUP, Rua das Estrelas, P-4150-762 Porto, Portugal*
[6]*Department of Physics, University of Oxford, Keble Road, Oxford OX1 3RH, UK*
[7]*Department of Physics and Astronomy, University of the Western Cape, Bellville 7535, South Africa*
[8]*NMES Faculty, King's College London, Strand Building, Strand, WC2R 2LS London, UK*

Accepted 2026 March 4. Received 2026 March 3; in original form 2025 September 2

ABSTRACT

Titan is regarded as a Solar system natural laboratory for studying atmospheric photochemistry and abiotic production of organic molecules on cold small exoplanets. Since the *Cassini-Huygens* mission ended, telescope observations enabled new detections of increasingly complex carbon-based molecules at infrared and sub-mm wavelengths, while the optical regime has been largely overlooked. Following a recent tentative detection of the 4050 Å absorption band of C_3 in Titan – a photochemical precursor to aromatic chemistry – in archived optical VLT-UVES spectra ($R\approx 60\,000$), this work presents a 8σ detection of the C_3 4050 Å absorption band in Titan from dedicated ultra-high-resolution VLT-ESPRESSO observations of Titan ($R\approx 190\,000$, highest spectral resolution observations of Titan in optical wavelengths ever). VLT-ESPRESSO spectrum is compared to a model spectrum of Titan, for varying C_3 abundances; a χ^2 curve is drawn to assess the agreement of non-solar spectral features with C_3 absorption when varying C_3 abundance; and a Bayesian Markov chain Monte Carlo (MCMC) fit between model and observed spectra is performed. χ^2 curve analysis yields an 8σ C_3 detection, consistent with a C_3 column density of $N = 1.5 \times 10^{13}$ cm^{-2}, whereas the MCMC fit retrieved a C_3 column density on Titan's atmosphere of $N = (1.47 \pm 0.30) \times 10^{13}$ cm^{-2} at 5σ, the same order of magnitude of predicted C_3 abundances by photochemical models, reaching ppm levels on Titan's mesosphere. This work showcases the usefulness of instruments and techniques originally dedicated to exoplanet research when applied to Solar system targets and science cases.

Key words: astrobiology – molecular data – instrumentation: spectrographs – methods: observational – planets and satellites: atmospheres – planets and satellites: individual: Titan.

1 INTRODUCTION

1.1 On Titan's atmosphere

Titan, with its dense and chemically rich atmosphere and likely subglacial water ocean, stands out amongst the icy moons as one of the most extensively studied bodies in the Solar system (S. M. Hörst 2017) (S. MacKenzie et al. 2021). The diversity and uniqueness of Titan's distinct environmental, physical, and chemical characteristics have sparked a long-lasting interest in the largest satellite of Saturn, covering a wide array of scientific areas, from atmospheric chemistry to planetary geology and even to astrobiology S. M. Hörst 2017; S. MacKenzie et al. 2021.

A major reason for Titan's uniqueness is the unusually large and dense atmosphere for an icy satellite, reaching Earth-like densities and pressures on its troposphere (A. Sánchez-Lavega 2011) and sharing the same major atmospheric constituent (N_2) with the Earth's atmosphere (S. M. Hörst 2017). The photochemical dissociation of atmospheric CH_4 (and to a lesser extent N_2) on Titan's upper atmosphere leads to a complex chain of photochemical reactions that give rise to a diverse set of increasingly complex hydrocarbons, nitriles and organic compounds (S. MacKenzie et al. 2021). The vast photochemical production of organic compounds on Titan creates precursors to the organic hazes that enshroud its atmosphere, a process akin to the one that is believed to have occurred on the early Earth (M. Trainer et al. 2006). While the extent of its contribution to the emergence of life on Earth is unclear, it is believed that the production of photochemical organic hazes could take place across the Galaxy on Titan-like exoplanets (G. Arney et al. 2017).

Understanding the chemical complexity of Titan's atmosphere has benefited from parallel contributions from observations and modelling work (S. M. Hörst 2017). Early remote sensing observations from *Voyager 1* and ground-based telescopes have hinted at the chemical complexity of Titan's atmosphere which motivated preliminary studies on the atmospheric production of organic molecules (Y. L. Yung, M. Allen & J. Pinto 1984). The *Cassini-*

★ E-mail: rafael.silva@ucl.ac.uk

Huygens space mission enabled an in-depth study of Titan's photochemical processes and products, characterizing profiles of higher-order hydrocarbons and nitriles (e.g. C_2N_2, HCN, HC_3N, C_4H_2 and C_3H_4; N. Teanby et al. 2009; A. Coustenis et al. 2010) as well as simple aromatic compounds like benzene (C_6H_6) (V. Vuitton, R. V. Yelle & J. Cui 2008).

Since the end of the *Cassini* mission in 2017, the observational study of Titan's atmosphere has been carried forward with several new molecular discoveries from ground-based sub-mm (e.g. detection of c-C_3H_2 with ALMA, C. Nixon et al. 2020) and infrared high-resolution observations (e.g. detection of CH_2CCH_2 with IRTF-TEXES; N. Lombardo et al. 2019). Recent space-based observations from near to mid-infrared observations with *James Webb Space Telescope* (*JWST*) have also contributed to this effort, directly detecting the methyl radical, CH_3, one of the main actors on Titan's atmospheric photochemistry (C. Nixon et al. 2025).

It is worth noticing that despite being less challenging than infrared observations due to the transparency of Earth's atmosphere, ground-based high-resolution observations of Titan in visible wavelengths have been largely overlooked (R. Rianço-Silva et al. 2024). One of the reasons behind this is the fact that most of the strongest molecular absorption features of the molecules present in Titan's atmosphere are present in the near and mid infrared spectral regions (C. Nixon et al. 2025). A notable exception to this is precisely the object of study of this work – the molecule of propadienediylidene (C_3) also known as tricarbon (A. Lynas-Gray et al. 2024).

1.2 On the molecule of C_3

Described for the first time in an astrophysical setting by A. Douglas (1951), on the active coma of a comet, propadienediylidene (or tricarbon, from here on, C_3) has ever since been found across a wide range of carbon-rich, energetic environments – in particular, interstellar dark clouds (M. R. Schmidt et al. 2014) and the atmospheres of carbon-rich stars (P. Swings, A. McKellar & K. N. Rao 1953). These early astrophysical detections of C_3 relied on its strong spectral features in the violet section of the visible spectrum at 4050 Å which L. Gausset et al. (1965) identified as the $\tilde{A}^1\Pi_u - \tilde{X}^1\Sigma_g^+$ 000–000 electronic transition. With the advent of very high-resolution spectroscopy, a continuous work of improvement of the resolution of molecular line lists of C_3 (A. Tanabashi et al. 2005) has allowed the detection of C_3 4050 Å absorption on the interstellar medium with visible high-resolution spectrographs such as VLT-UVES with resolving powers of $R > 60\,000$ (e.g. M. R. Schmidt et al. 2014; H. Fan et al. 2024).

The thought of Titan's upper atmosphere as a carbon-rich energetic environment with complex photochemical networks has led modelling works to consider the effect of highly unsaturated C_3-hydrocarbons on their photochemical networks. Remarkably, E. Hébrard et al. (2013) and M. Dobrijevic et al. (2016) predicted that C_3 could be among the most abundant three carbon species present in the upper atmosphere of Titan, reaching molar ratios of the order of ppm at 400 km (lower mesosphere) of tens of ppm at altitudes of 800 km (upper mesosphere) (E. Hébrard et al. 2013) – equivalent to a maximum predicted column density of C_3 in Titan's atmosphere of 5×10^{13} cm^{-2}. These relative abundances are comparable with those of the most abundant detected three-carbon hydrocarbons, such as propane (C_3H_8) at the ppm level across Titan's stratosphere and mesosphere (M. Dobrijevic et al. 2016).

Indeed and unlike more chemically stable three-carbon hydrocarbon species (C_3H_8, C_3H_6, CH_2CCH_2 and CH_3CCH) which are observed in Titan's stratosphere (N. Lombardo et al. 2019), C_3 is predicted to be significantly depleted in Titan's stratosphere, with relative abundances plummeting below ppt levels at altitudes lower than 300 km (E. Hébrard et al. 2013). This effect has also been described and observed for c-C_3H_2 (C. Nixon et al. 2020 and K. Willacy et al. 2022), which is the most similar species to C_3 detected in Titan up to this point. Possible reasons for this distinct vertical profile peaking in relative abundance at the upper mesosphere and stratospheric depletion for both C_3 and c-C_3H_2 could be traced to the increase in the reaction with H atoms in the lower mesosphere and stratosphere, described in (M. Dobrijevic et al. 2016) and (K. Willacy et al. 2022).

The C_3 molecule is particularly interesting for the evolution of chemical complexity in Titan's atmosphere, as it is thought to play a role on the production of aromatic chemistry in Titan (J. Loison, M. Dobrijevic & K. Hickson 2019) since its reaction with the CH_3 radical significantly impacts the production of C_4H_2 (A. Mebel et al. 2023). C_4H_2 is then a direct precursor of benzene and other aromatics in Titan (including PAH) (J. Loison et al. 2019) which are known to play a pivotal role in prebiotic processes (P. Ehrenfreund et al. 2006). Hence, given the great interest for astrobiology of the atmospheric production of aromatic species, it is critical to gain understanding of the many 'missing links' – such as the reaction rates of $C_3 + CH_3$ which are challenging to study experimentally (A. Mebel et al. 2023). Detecting and retrieving the atmospheric abundance of C_3 in Titan will therefore provide key observational constraints to the models that attempt to describe the production of prebiotic molecules on the atmosphere of Titan (J. Loison et al. 2019).

However, in spite of its importance and high predicted abundance in Titan's mesosphere, no direct and conclusive detection of C_3 has been reported thus far. Possible reasons for this might be connected to the lack of an infrared, detailed line list of C_3 – recently addressed by the ExoMol project (A. Lynas-Gray et al. 2024) – and the largely overlooked visible spectrum of Titan, where the strongest spectrum features of C_3 are present (R. Rianço-Silva et al. 2024). The sole indirect evidence for the presence of C_3 in Titan stems from the INMS peak at 37 m/z units attributed to the C_3H^+ (V. Vuitton, R. V. Yelle & M. McEwan 2007) which is the most likely loss mechanism for C_3 (M. Dobrijevic et al. 2016).

Apart from this, a recent study with VLT-UVES has claimed a tentative detection of the C_3 4050 Å-band in Titan's atmosphere from very high resolution visible spectroscopy (R. Rianço-Silva et al. 2024). Despite this encouraging result, which was consistent with the presence of C_3 in Titan at a column density of 10^{13} cm^{-2}, the small number and a low signal-to-noise ratio (SNR) of detected spectral features of C_3 in R. Rianço-Silva et al. (2024) require further observations at increased spectral resolution and SNR to allow confirming the detection of C_3 in Titan. This is the purpose of this work which is organized as follows: In Section 2 we describe the VLT-ESPRESSO observations of Titan and their data reduction. In Section 3 we describe our model for Titan's spectrum with C_3 absorption. In Section 4 we show our observational results and compare them to the spectral model of Titan through a χ^2 analysis and through a Markov chain Monte Carlo (MCMC) Bayesian retrieval, and in Section 5 we discuss and conclude.

2 OBSERVATIONS AND DATA REDUCTION

2.1 Observations

The dedicated observations used for this work were obtained with the European Southern Observatory's Very Large Telescope (VLT) ESPRESSO (Échelle SPectrograph for Rocky Exoplanets and Stable Spectroscopy Observations) instrument. VLT-ESPRESSO is a visible, high-resolution, fibre-fed, cross-dispersed, échelle spectrograph at the Incoherent Combined-Coudé Laboratory (ICCL) of the VLT, allowing this instrument to receive light from any of the four 8 m-class Unit Telescopes (F. Pepe et al. 2014). Although originally built with the goal of searching for and characterizing exoplanets, VLT-ESPRESSO has already proven to be a very useful instrument for Solar system science, having enabled Doppler velocimetry studies of the atmosphere of Jupiter (P. Machado et al. 2023).

Titan was observed for 2 h 20 min with VLT-ESPRESSO, starting at 00:17 UTC on 2024 December 4, as part of the ESO observing program 114.277N, using the ultra-high-resolution (UHR) mode of VLT-ESPRESSO (F. Pepe et al. 2021). This is the highest spectral resolution mode available with VLT-ESPRESSO, reaching a resolving power of 190 000 – making these the observations of Titan at the highest spectral resolution ever done in optical wavelengths. During the course of the observation the seeing (FWHM) was below 0.8 arcsec and the sky was clear. Titan's solid body (diameter = 5150 km) corresponded on the observation night to an apparent angular diameter of 0.74 arcsec. However, due to its thick, opaque atmosphere, Titan's optical radius at $\lambda = 400$ nm is about 300 km high in its atmosphere (R. Lorenz et al. 1999). This yields a Titan optical diameter of 5750 km at $\lambda = 400$ nm, corresponding to an apparent angular diameter of 0.826 arcsec on the observation night. This implies that the VLT-ESPRESSO 0.5 arcsec fibre was fully covered by Titan's disc – with implications for modelling Titan's atmosphere described In Appendix B. At the time, Titan had an apparent V-band magnitude of +8.62, a surface brightness of 7.71 mag arcsec^{-2} and an illuminated fraction of 99.73 per cent. Target ephemerides were obtained from the Horizons System – Solar System Dynamics Ephemerides Calculator from NASA/JPL (J. Giorgini et al. 1996).

The set of seven exposures (each 20 min long) of Titan enabled a coverage of the entire visible, backscattered spectrum of Titan (at the wavelength range of 378.2–788.7 nm), reaching an SNR of 60 at 405 nm on each exposure. This would imply a total SNR close to 100, after stacking the seven exposures.

2.2 Data reduction

2.2.1 Removing telluric effects and stacking exposures

The data were reduced with ESPRESSO Data Reduction Software version 3.3.0. After obtaining individual flux-calibrated spectra for each Titan exposure, we removed the effects of the variation of air mass in multiple exposures, which are evident in Fig. A1. To do so, we obtained a third-degree polynomial fit of the division of each exposure's Titan spectrum by the spectrum of the exposure at the lowest airmass (see Fig. A2). The spectrum of each exposure was then divided by the respective normalized polynomial fit to remove the effect of varying air mass on the spectral continuum (a value between 0 and 1 for each spectral wavelength bin). The spectral flux errors, $\delta S_{\lambda,i}$, associated with the ith exposure spectral flux measurement, $S_{\lambda,i}$, were obtained in a similar fashion: each exposure's spectral flux error ($\delta S_{\lambda,i}$) was divided by the respective normalized polynomial fit to the airmass (a value between 0 and 1 for each wavelength bin), maintaining each exposure's SNR after removing the effect of varying airmass across exposures. After this, the Titan spectra (corrected for airmass variation, as shown in Fig. A3) were averaged together to obtain a single Titan spectrum, S_λ, for the entire observation night (equation 1).

$$S_\lambda = \frac{1}{N}\sum_{i}^{N} S_{\lambda,i} \tag{1}$$

The respective spectral flux errors for each i exposure were also combined into a single spectral flux error per wavelength bin, δS_λ, as shown in equation (2), the equation for the standard error of the mean, which depends on two terms: the first term accounts for the average of the intrinsic spectral flux error ($\delta S_{\lambda,i}$) per wavelength bin, per exposure, i.e. the spectral flux error associated with each spectral flux measurement per each exposure. The second term depends on the scatter of the spectral flux values per exposure and wavelength bin ($S_{\lambda,i}$) around their average, obtained in equation (1), corresponding to the variance scatter between the multiple stacked exposures (s^2). Both terms are summed in quadrature in equation (2), allowing us to account for both the intrinsic uncertainties in each exposure as well as the scatter between the different exposures. Stacking these spectra increased the total SNR, reaching ≈ 100 at 405 nm, as shown in Fig. A4.

$$\delta S_\lambda = \sqrt{\frac{1}{N}\left(\frac{1}{N}\sum_{i=1}^{N}\delta S_{\lambda,i}^2 + s^2\right)}, \text{ where } s^2 = \frac{1}{N-1}\sum_{i=1}^{N}(S_{\lambda,i} - S_\lambda)^2 \tag{2}$$

One extra step in data reduction involves normalizing the average Titan spectrum by its spectral continuum, to make it directly comparable with the normalized solar spectrum as described in Section 3. To do so, we obtain the spectrum continuum using a Savitzky–Golay filter (A. Savitzky & M. Golay 1964) as shown in Fig. A5.

It is also worth noticing that the spectral flux errors per exposure are dominated by the photonic error, as expected from ESPRESSO's exposure time calculator (ETC) (F. Pepe et al. 2021), where for the conditions of these observations and for a target akin to Titan, the combined contributions to the error from sky, dark current and read-out-noise are below 2 per cent of the photonic noise from Titan's brightness. Hence, an SNR roughly scales with the square root of the observation time, as these observations are photon-noise limited.

After removing the continuum telluric contributions to the observed spectrum, we solely focus on the spectral region of interest corresponding to the C_3 $\tilde{A}^1\Pi_u - \tilde{X}^1\Sigma_g^+$ 000–000 band, on the narrow wavelength region between 4040 Å and 4060 Å as shown in Fig. A6. This allows a search for possible telluric absorption or emission lines that could have contaminated the spectral section that is crucial for this analysis. Following the approach of J. Dias, P. Machado & J. Ribeiro (2022) for high spectral resolution observations of other Solar system targets, we used NASA's open-access Planetary Spectrum Generator (PSG) radiative transfer suite to simulate the transmission of the Earth's atmosphere (G. Villanueva et al. 2018) for VLT. From the simulated transmission spectrum of Earth's atmosphere at the ESPRESSO UHR mode resolution (shown in grey in Fig. 1), no telluric absorption or emission line causing a variation of transmission above 0.01 per cent is present in the 4040 Å and 4060 Å wavelength range, well below the sensitivity allowed by a high SNR of these observations, thus discarding the need for additional telluric correction.

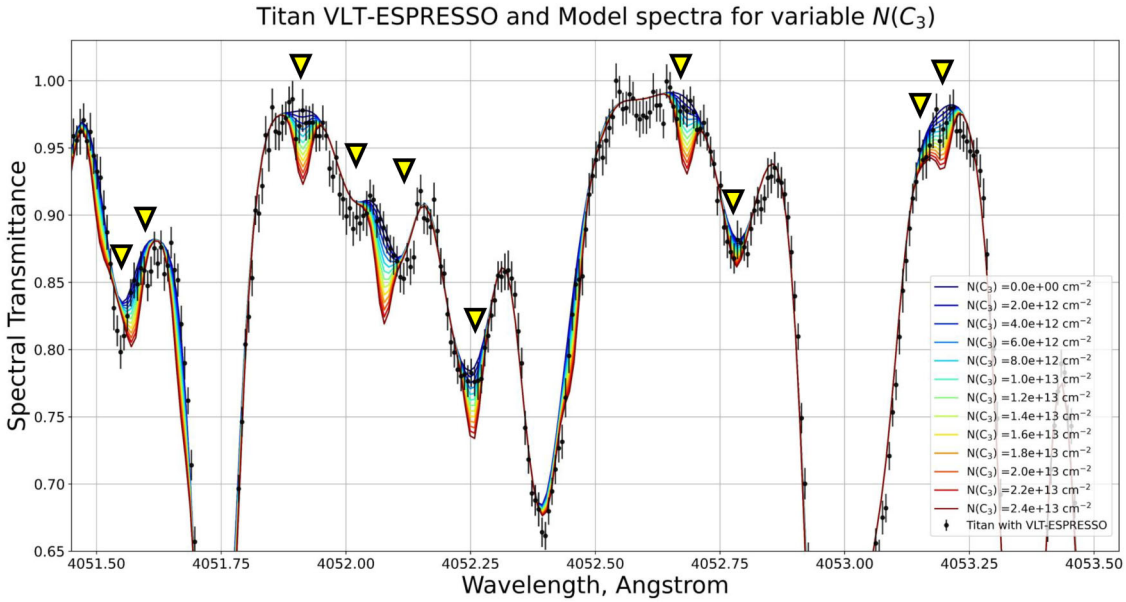

Figure 1. VLT-ESPRESSO normalized spectrum of Titan (black data points) at the spectral region of interest for the $\tilde{A}^1\Pi_u - \tilde{X}^1\Sigma_g^+$ 000–000 band of C_3 compared to an array of spectral models of Titan with varying column densities of C_3 (N). Spectral models based on the H. Fan et al. (2024) C_3 line list. Telluric transmission obtained from Planetary Spectrum Generator, shifted upwards by 1 per cent for clarity (G. Villanueva et al. 2018). The triangles mark the identified spectral features we associate with C_3 absorption features, described in Table D1.

2.2.2 Removing Doppler shifts

A key step to take into account when dealing with observations of Solar system objects in high spectral resolution is the correction of the orbital Doppler shift. This Doppler shift is a consequence of the relative motions between the observer (on Earth) and the observed body, causing a shift on the observed wavelengths $\Delta\lambda$ given by

$$\Delta\lambda = \lambda_0 \frac{v}{c}, \tag{3}$$

where λ_0 is the rest-frame wavelength, before Doppler shift occurs. The absorption lines that we aim to detect on Titan's atmospheric spectra ought to occur on Titan's rest frame. Hence, it is key to shift the observed spectrum to Titan's rest frame, by subtracting from each wavelength bin the associated Doppler shift, given by equation (3). For reference, during the observation, Titan's radial velocity with respect to the observer at VLT was 5.33 km s^{-1}, towards the observer (from J. Giorgini et al. 1996), which amounts to a Doppler shift of 0.072 Å at 4050 Å.

3 MODELLING C_3 ABSORPTION IN TITAN

When analysing the observed spectrum, it makes sense to directly compare it with the modelled spectrum of Titan in the wavelength regions of interest. Here we follow the approach used in R. Rianço-Silva et al. (2024), whereby this very short wavelength span of Titan's spectrum (2 nm-wide) is modelled as a normalized backscattered solar spectrum upon which occurs the C_3 line absorption. This is a valid approximation since

(i) The absorption of C_3 is expected to occur on the upper layers of Titan's atmosphere (altitudes above 400 km), significantly above the optical radius of Titan at 405 nm (below 250 km, from R. Lorenz et al. 1999) where backscatter occurs.

(ii) The spectrum of Titan in this short wavelength section is dominated by continuum haze absorption and scatter, which do not produce high-resolution features. In R. Rianço-Silva et al. (2024), it was shown that the continuum haze absorption of Titan varies by less than 0.04 per cent per Ångstrom over the 400–500 nm region, which is negligible for the wavelength range and SNR of the observed spectrum.

(iii) There are no other known absorbing gases in Titan's atmosphere (apart from C_3) that showcase absorption lines on the 4040–4060 Å wavelength range, as was also shown in R. Rianço-Silva et al. (2024).

Hence, we model the UHR spectrum of Titan in the 4040–4060 Å wavelength range as a product of a UHR solar spectrum (the R. Kurucz (2006) solar spectrum at $R = 500\,000$, with a spectral resolution degraded to ESPRESSO UHR $R = 190\,000$) multiplied by the modelled C_3 transmission spectrum, $M(\lambda, T, N)$.

The C_3 transmission spectrum, $M(\lambda, T, N)$, was based on the most recent line list of C_3 covering its $\tilde{A}^1\Pi_u - \tilde{X}^1\Sigma_g^+$ 000–000 band, by H. Fan et al. (2024), by combining multiple previous line lists, such as the ones from A. Tanabashi et al. (2005) and M. R. Schmidt et al. (2014). It is worth noticing that these line lists were obtained through comparison with observational data from VLT-UVES, with a spectral resolution of $R \approx 80\,000$ (H. Dekker et al. 2000), less than half of the UHR mode of VLT-ESPRESSO. These line lists solely contain the following information for each C_3 line: its wavelength, λ_j, its corresponding transition within the P, Q, and R branches (associated with its J-level), and its oscillator strength, f_j (H. Fan et al. 2024).

The first step to model the C_3 transmission spectrum in Titan's atmosphere is to obtain its partition function across the multiple molecular energy states (J) associated with the vibronic transitions. Assuming thermal equilibrium, this partition is given by a Boltzmann distribution as shown in equation (4), where B = 0.431 cm^{-1}, from A. Tanabashi et al. (2005). For the partition function sum at the denominator of equation (4), k are summed

across all the observed rotational levels, from H. Fan et al. (2024).

$$p(J,T) = \frac{(2J+1)\exp\left[-\frac{BJ(J+1)}{k_B T}\right]}{\sum_k \left((2k+1)\exp\left[-\frac{Bk(k+1)}{k_B T}\right]\right)}. \quad (4)$$

This distribution of the gas molecules across the multiple states (J) is used to calculate the line strength, S_j, of each transition from the wavelengths, λ_j, and oscillator strengths, f_j, provided in the C_3 line lists, as shown in equation (5) (A. Sánchez-Lavega 2011). Considering thermal equilibrium, the line profiles of individual absorption lines of C_3 are Gaussian and given by $G_j(\lambda, T)$, as described in equation (6), where the Doppler broadening coefficient, $\gamma_{j,D}(T)$, is given by equation (7), which depend on m_{C_3}, the mass of the C_3 molecule.

$$S_j = \frac{e^2\lambda_j^2}{4m_e c^2 \varepsilon_0} p(J,T).f_j \quad (5)$$

$$G_j(\lambda,T) = \frac{S_j}{\gamma_{j,D}(T).\sqrt{\pi}}.\exp\left[-\left(\frac{\lambda-\lambda_j}{\gamma_{j,D}(T)}\right)^2\right] \quad (6)$$

$$\gamma_{j,D}(T) = \frac{\lambda_j}{c}\sqrt{\frac{2k_B T}{m_{C_3}}}. \quad (7)$$

Finally, the optical depth profile of each absorption line, $\tau_j(\lambda, T, N)$ is given by the product of the line profile $G_j(\lambda, T)$ and the column density of C_3 in Titan's atmosphere, N and a factor of $\tilde{A} \simeq 2.2155$ which accounts for the spherical geometry of Titan's atmosphere in equation (8). This accounts for the varying slant paths of photons across the illuminated disc, by adopting an effective path length enhancement factor of $\tilde{A} \simeq 2.2155$, integrating the effect of the varying airmass over the observed disc of Titan compared to the vertical two-way path at the disc centre. This factor is an approximation for a Lambertian sphere, where photons near the planetary limb traverse a longer atmospheric column (P. Palmer et al. 2001).

$$\tau_j(\lambda,T,N) \approx \tilde{A} G_j(\lambda,T) N. \quad (8)$$

In order to get the complete model transmission spectrum of the C_3 absorption band on Titan, $M(\lambda, T, N)$, we multiply all of the individual lines (of all absorption lines identified in H. Fan et al. 2024) transmission profiles, $M_j(\lambda, T, N)$, which result from the Beer–Lambert law considering a two-way path of light down to the optically thick layer where backscattering is assumed to occur (effective airmass of $\tilde{A} \simeq 2.2155$, described above), as shown in equation (9).

$$M(\lambda,T,N) = \prod_j M_j(\lambda,T,N) = \prod_j e^{-\tau_j(\lambda,T,N)} \approx \prod_j e^{-\tilde{A}G_j(\lambda,T)N}. \quad (9)$$

Finally, the synthetic spectrum of Titan is obtained by multiplying the Transmission spectrum of C_3 by the normalized solar spectrum, and then convolved with a gaussian profile with a full width at half-maximum (FWHM) equal to the VLT-ESPRESSO spectral resolution, so that the synthetic spectrum of Titan is showcased at the same spectral resolution as the observed data – again following the procedure described in R. Rianço-Silva et al. (2024).

4 RESULTS AND DISCUSSION

4.1 Comparing model spectra and observations

In order to compare the observed VLT-ESPRESSO spectrum of Titan with the synthetic model spectra with C_3 absorption, we have created an array of model spectra by varying the column density of C_3, N, from 0 to 3×10^{13} cm^{-2}, with 2×10^{12} cm^{-2} steps and assuming $T = 200$K – the temperature of Titan's atmosphere at an altitude of 400 km (S. M. Hörst 2017). This comparison is shown in Fig. 1.

Although the most prominent features in this region of the spectrum are the backscattered solar absorption lines, it is noteworthy that several features in the VLT-ESPRESSO spectrum of Titan match those in the simulated Titan spectrum that include modelled C_3 absorption lines. A comparison between modelled and observed spectral features is provided in Table D1. These features deviate from the normalized solar spectrum, which represents Titan's baseline spectrum without any C_3 absorption. This is particularly evident for the spectral features at 4052.27 Å, 4052.77 Å, and 4053.19 Å. However, it is also noticeable that in some cases, the C_3 absorption lines in the modelled spectra are shifted by a few hundredths of Ångstrom from the observed spectral features that diverge away from the normalized solar spectrum. This is particularly evident for the spectral features at 4051.60 Å, 4051.90 Å, 4052.11 Å, and 4052.67 Å.

A possible explanation for this are uncertainties on the C_3 line lists used to model the C_3 absorption spectrum, taken from A. Tanabashi et al. (2005), M. R. Schmidt et al. (2014) and H. Fan et al. (2024). This is since the C_3 line lists were empirically obtained and validated through the observation of interstellar C_3 absorption lines using VLT-UVES observations with resolving powers of $R \approx 80\,000$ (H. Fan et al. 2024). This implies a spectral resolution for past VLT-UVES observations no better than $\Delta\lambda = R/\lambda$, or $\Delta\lambda = 0.05$ Å at $\lambda = 4050$ Å, which compares to a VLT-ESPRESSO spectral resolution at the UHR mode of $\Delta\lambda = 0.02$ Å. It is possible that this observation with improved resolving power requires a correction in some of the wavelengths associated with the centre of some of the C_3 lines, as was done in past works following an improvement in spectral resolution compared to the previous literature (A. Tanabashi et al. 2005; M. R. Schmidt et al. 2014; H. Fan et al. 2024).

4.2 $\Delta\chi^2$ analysis

To assess whether non-zero values of modelled C_3 absorption actually return an improvement to the quality of the model fit to the VLT-ESPRESSO data, we have calculated a $\Delta\chi^2$ curve to the model fit to the data, as a function of column density of absorbing C_3, $N(C_3)$. This analysis follows the approach of C. Nixon et al. (2020), where χ^2 is defined by equation (10), with S_λ corresponding to the VLT-ESPRESSO measured Titan spectral flux, $M_\lambda(N)$ corresponding to the modelled Titan flux as a function of C_3 column density, N, and δS_λ corresponding to the VLT-ESPRESSO measured uncertainty (i.e. the measured spectral flux at wavelength λ by VLT-ESPRESSO is given by $S_\lambda \pm \delta S_\lambda$).

$$\chi^2(N) = \sum_\lambda \left(\frac{S_\lambda - M_\lambda(N)}{\delta S_\lambda}\right)^2, \quad \Delta\chi^2(N) = \chi^2(N) - \chi^2(N=0). \quad (10)$$

Based on the framework of C. Nixon et al. (2020), we calculate the difference of χ^2, $\Delta\chi^2(N)$, by subtracting $\chi^2(N=0)$ (the χ^2

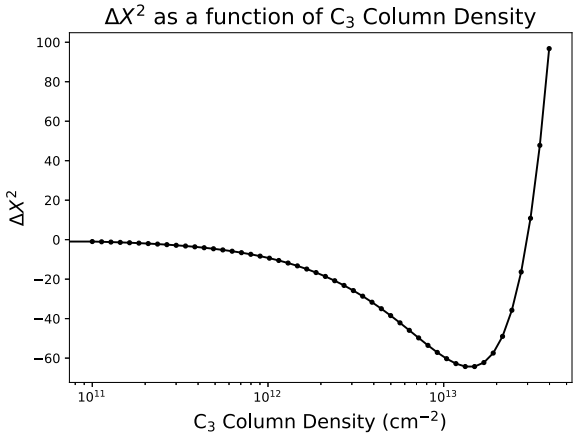

Figure 2. $\Delta\chi^2$ curve as a function of column density of C_3, $N(C_3)$, following the approach of (C. Nixon et al. 2020). This plot shows an increase in the quality of the spectrum as the column density approaches $N(C_3) = 1.5 \times 10^{13}$ cm^{-2}, suggesting a detection of C_3 in Titan.

value for the no C_3 case) to each calculated $\chi^2(N)$. If the spectral fit improves with the inclusion of C_3 absorption in the model, we would expect $\Delta\chi^2(N)$ to decrease until a strong minimum is reached – which should indicate the $N(C_3)$ for which the best model fit is obtained. It should also be noted that unlike for standard χ^2 analysis, the approach followed by C. Nixon et al. (2020) is indicative of a good spectral fit for $\chi^2 \sim n$, where n is the number of data points used in the fit, set at $n = 1000$.

In Fig. 2 we show the $\Delta\chi^2(N)$ curve we obtained by calculating the $\Delta\chi^2(N)$ for a set of 50 values of N spaced in logspace from $N = 10^{11}$ cm^{-2} to $N = 10^{14}$ cm^{-2}. The $\chi^2(N = 0)$ in this distribution is 1080, which secures that the model fit to the spectral is good. As would be expected for a C_3 detection, we observe a strong minimum emerging in the $\Delta\chi^2(N)$ curve as N increases, implying that adding C_3 absorption to the spectral model improves the quality of the spectral fit (up to an inversion point on this trend, a χ^2 minimum). The $\Delta\chi^2(N)$ strong minimum is observed at $N(C_3) = 1.5 \times 10^{13}$ cm^{-2}, a column density in agreement with the past tentative estimates of C_3 abundance in Titan's upper atmosphere (R. Rianço-Silva et al. 2024).

Furthermore, the local minimum's depth in $\Delta\chi^2$ is of -64.2. Again, following the approach of C. Nixon et al. (2020), we retrieve this result's significance as $\sqrt{64.2}$, thus yielding a detection significance of C_3 in Titan of 8.0σ.

4.3 MCMC likelihood fit to the spectrum

In order to further and independently clarify this detection of C_3 in Titan and retrieve the atmospheric abundance of C_3 in a more robust way, we turn to Bayesian statistics as is standard procedure in atmospheric retrievals based on planetary spectra, in particular for atmospheric retrievals on exoplanet spectra (e.g. I. P. Waldmann et al. 2015, J. Taylor et al. 2023, Q. Xue et al. 2024). Although not widely used for Solar system targets, where SNRs are often high enough to produce unequivocal detections of individual spectral lines, Bayesian statistical analysis provides a useful tool to examine situations such as this, where absorption features are of the order of magnitude of errorbars (I. P. Waldmann et al. 2015) as is the case here.

Taking as a starting point our simple model spectrum of Titan, $M_\lambda(T, N)$, which considers a single absorbing layer of C_3, the 2

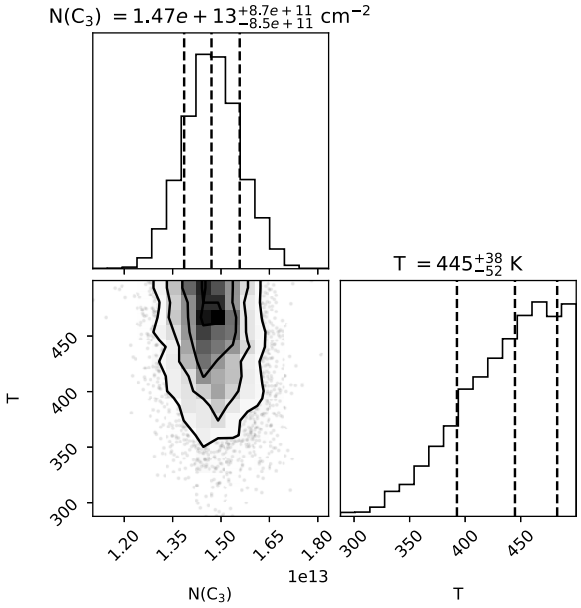

Figure 3. Posterior plots from the MCMC fit to the VLT-ESPRESSO spectrum of Titan. Fit for the column density of C_3 (N) and for the temperature (T). Retrieved values showcased with 1σ errorbars. Contour plots on the 2D histogram correspond to the 0.5σ, 1σ, 1.5σ, and 2σ confidence regions for a 2D Gaussian distribution. Histogram y-axis correspond to the retrieved probability distribution, unitless.

free variables that we aim to retrieve from the spectrum are the column density of C_3, $N(C_3)$, and its temperature, T. In order to sample and assess the probability distribution of the fits to the multiple models to the spectral data, we use an MCMC ensemble sampler based on the EMCEE PYTHON package (D. Foreman-Mackey et al. 2013).

For an MCMC ensemble sampler, with spectral data points described by λ, S_λ, and δS_λ (wavelength, measured spectral flux, and respective spectral flux error, respectively), and fitted variables with N and T, the Bayesian argument to the spectral fit is given by equation (11)

$$p(N, T|\lambda, S_\lambda, \delta S_\lambda) \propto p(N, T).p(S_\lambda|\lambda, \delta S_\lambda, N, T). \quad (11)$$

From equation (11) we get that the probability distribution function of the retrieved variables N and T applied to the spectral data set is proportional to its prior function $p(N, T)$ and the likelihood function, $p(S_\lambda|\lambda, \delta S_\lambda, N, T)$, following D. Foreman-Mackey et al. (2013) and I. P. Waldmann et al. (2015). The priors for N and T were defined as uniform priors with bounds 0 and 10^{14} cm^{-2} and 0 to 500 K, respectively. These wide prior ranges allow for the MCMC sampler to explore a wide range of realistic values for these variables' parameter space. Also following D. Foreman-Mackey et al. (2013) and I. P. Waldmann et al. (2015), the likelihood function can be defined as a log-likelihood function, given by equation (12), which we aim to maximize.

$$\log(\mathcal{L}) = -\frac{1}{2}\sum_\lambda \left[\frac{(S_\lambda - M_\lambda(N, T))^2}{(\delta S_\lambda)^2}\right] - \log\left(\sqrt{2\pi(\delta S_\lambda)^2}\right). \quad (12)$$

This MCMC likelihood fit to the VLT-ESPRESSO spectrum of Titan was run for 5000 iterations, resulting in the posterior plots of Fig. 3. Unlike the χ^2 curve shown in Section 4.2, retrieval posterior plots do not show the quality of the spectral fit in units of noise standard deviations. Instead, these correspond to

probability distribution histograms, showcasing the variable (N and T) values for which the spectral fit log-likelihood function is maximized. It is their distribution as a function of the assessed free parameters (N and T) that yields the most likely value for these variables (the histogram's median) as well as the retrieved value's errorbars (based on the standard deviations of the probability distribution; I. P. Waldmann et al. 2015). These posterior plots showcase a good consistency in the model's fit to the VLT-ESPRESSO spectrum of Titan for C_3 column density, allowing constraints to be placed on the abundance of C_3. Based on the posterior probability distribution to the MCMC fit and using the original H. Fan et al. (2024) C_3 line list, we retrieve a column density of C_3 in Titan of $N = (1.47 \pm 0.09) \times 10^{13}$ cm^{-2} and an associated temperature of $T = 445^{+38}_{-52}$ K, for 1σ uncertainties, as shown in the histograms of Fig. 3.

The retrieved values for 3σ uncertainties are $N = \left(1.47^{+0.25}_{-0.26}\right) \times 10^{13}$ cm^{-2} and an associated temperature of $T = 445^{+57}_{-134}$ K. For 5σ uncertainties, we get $N = (1.47 \pm 0.30) \times 10^{13}$ cm^{-2} and an associated temperature of $T = 445^{+58}_{-171}$ K. The posterior plot histogram showcases nearly symmetrical errorbars for the retrieval of C_3 column density, with errorbars confidently excluding the $N = 0$ scenario (equivalent to no C_3 on Titan). This further suggests the detection of C_3 on Titan's upper atmosphere with a confidence above 5σ, which is the standard to claim a new detection.

The histogram concerning the retrieval of T is not symmetrical, presenting a heavier tail skewed to higher temperature values revealing a challenging constraint in the temperature on this retrieval. Alongside the larger relative uncertainties in the temperature (uncertainties close to 50 per cent for the retrieved T at 5σ), this skewed distribution suggests a lower sensitivity to temperature on this fit. It may result as a consequence of the approximations applied to this model, in particular regarding thermal equilibrium and a constant temperature across the entire absorbing layer of C_3 which deviates from observed temperature profiles of Titan (K. Willacy et al. 2022). It may also stem from the aforementioned putative errors in some C_3 line positions in H. Fan et al. (2024) which would become more evident at these unprecedented spectral resolutions. Indeed, given the wide parameter range which this retrieval allowed for T (0K to 500K), it can be argued that the retrieval could have tended towards higher temperatures in order to enable substantial line broadening which would approximate the model fit to the slightly offset spectral features. In Appendix E we test whether a slightly adapted line list for C_3, based on the original H. Fan et al. (2024) line list, provides a better constrained posterior plot for T. This is verified in the posterior plots of Fig. E1 – pointing towards a possible improvement of the available C_3 line list, based on the fact that C_3 is clearly detected from an independent method, as was the χ^2 curve using the original line list. These small shifts that we suggest applying to the original H. Fan et al. (2024) C_3 line list are provided at the last column of Table D1. Despite this, the retrieved temperature's large uncertainties broadly match the maximum expected temperature for the altitude where the highest abundance of C_3 was predicted to occur – at an altitude of 400 km (E. Hébrard et al. 2013) (M. Dobrijevic et al. 2016), with a temperature of about 200K (S. M. Hörst 2017).

Nonetheless, these Bayesian retrievals also enable us to fit T to more physically motivated values (in our case, T = 200K, from S. M. Hörst 2017), which is helpful to test if even without the aforementioned non-physical line broadening enabled by the retrieval, the fit is still able to provide a 5σ detection of C_3. The result of such a fit is showcased in Fig. 4. It also shows a well-constrained retrieval for $N(C_3)$, with $N(C_3) = (1.38 \pm 0.09) \times 10^{13}$ cm^{-2} at 1σ, $N(C_3) = \left(1.38^{+0.26}_{-0.27}\right) \times 10^{13}$ cm^{-2} at 3σ and $N(C_3) = \left(1.38^{+0.36}_{-0.35}\right) \times 10^{13}$ cm^{-2} at 5σ, for T fixed at 200K. This retrieved value matches the results obtained by the χ^2 fit and the MCMC retrieval for N and T, which further confirms the detection described above, when fixing the temperature value, as the $N(C_3) = 0$ scenario is excluded at 5σ.

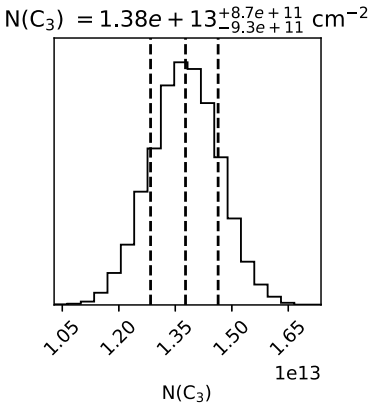

Figure 4. Posterior plots from the MCMC fit to the VLT-ESPRESSO spectrum of Titan. Fit for the column density of C_3 (N) for a fixed temperature value of $T = 200$K. Retrieved value showcased with 1σ errorbar. Histogram y-axis correspond to the retrieved probability distribution, unitless.

A plot showcasing the best-fitting model for this VLT-ESPRESSO spectrum of Titan obtained from the best-fitting parameter values for $N(C_3)$ and T, 3σ respective uncertainties, compared with the backscattered solar spectrum (a proxy for Titan's spectrum with no C_3 absorption), is shown in Fig. 5. This best-fitting plot with respective uncertainties further highlights the observed spectrum's deviation from the solar spectrum on the wavelengths subject to C_3 absorption – further confirming the detection of C_3 on Titan. In Appendix C, particularly in Fig. C1, we showcase the residual plots relative to the observed spectrum and the MCMC best-fitting spectral model – and one residuals plot relative to the spectral model with no C_3. As expected, the best-fitting MCMC spectral model (with C_3) improves the fit, decreasing the residual's deviation to closer to zero.

Interestingly, the retrieved column density for C_3 in Titan matches the estimated column density value found at the first tentative detection of C_3 in Titan with VLT-UVES in R. Rianço-Silva et al. (2024), and within the predicted upper and lower limits for $N(C_3)$ from M. Dobrijevic et al. (2016), which suggested C_3 column densities across Titan's mesosphere from 5×10^{12} cm^{-2} to 5×10^{13} cm^{-2}.

5 CONCLUSIONS

In this work, we have obtained and analysed VLT-ESPRESSO high-resolution visible spectra of Titan – which are to date, the visible spectra of Titan at the highest spectral resolution ever obtained. This unprecedented spectral resolution has enabled an increased sensitivity within the short wavelength range of interest for the search for C_3 absorption features, mostly in the 4050–4055 Å range, as compared to previous high-resolution observations of Titan (R. Rianço-Silva et al. 2024). Most importantly, this increased spectral resolution and sensitivity enabled

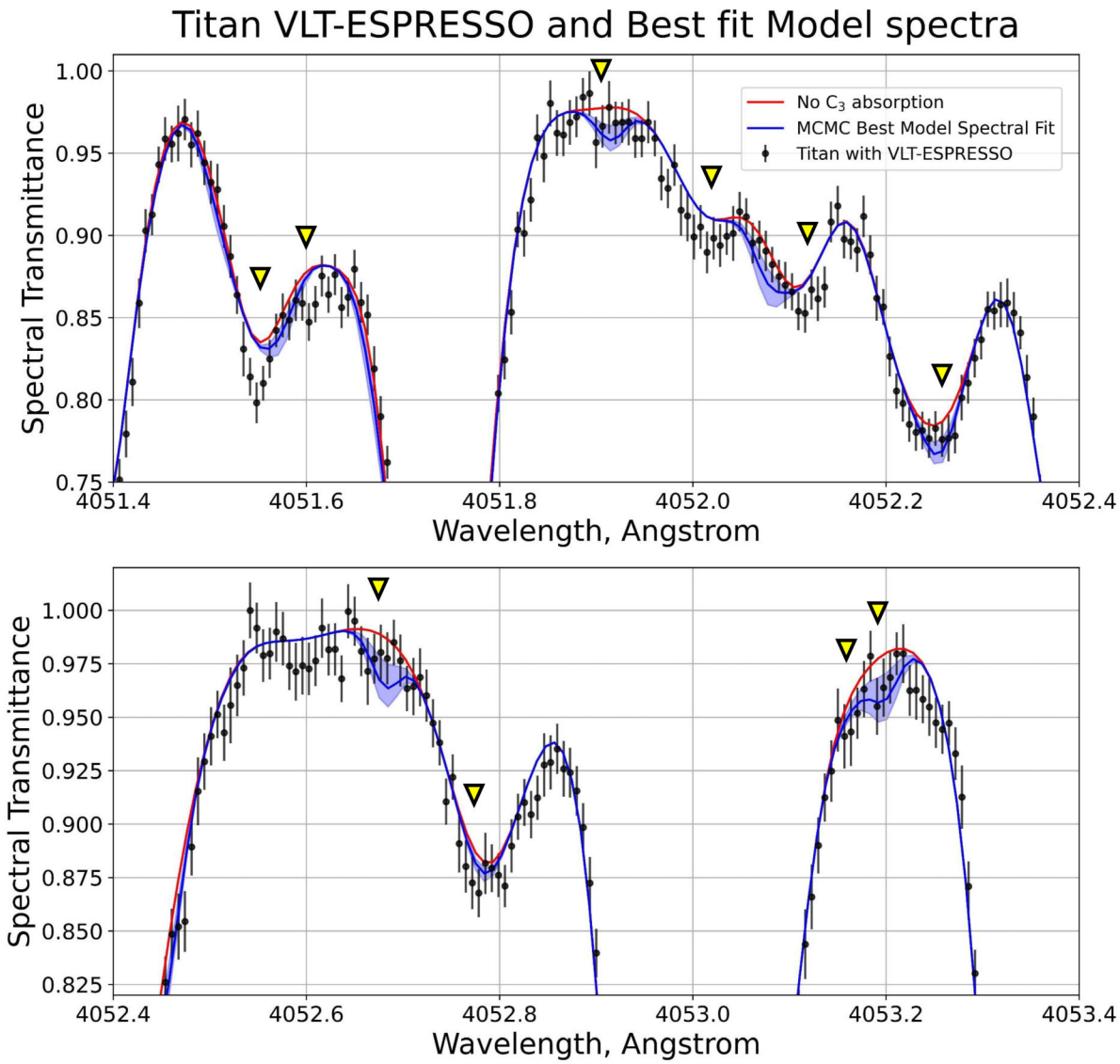

Figure 5. VLT-ESPRESSO normalized spectrum of Titan (black data points) at the spectral region of interest for the $\tilde{A}^1\Pi_u - \tilde{X}^1\Sigma_g^+$ 000–000 band of C_3 compared to the backscattered solar spectrum (a proxy for Titan's spectrum with no C_3 absorption, in red) and to the best-fitting model obtained from the MCMC likelihood fit, associated with the retrieved values for $N(C_3)$ and T, in blue. The shaded blue area corresponds to the best-fitting model uncertainty based on the retrieved $N(C_3)$ and T values with 3σ errorbars. The triangles mark the identified spectral features we associate with C_3 absorption features, described in Table D1.

by VLT-ESPRESSO disentangles more effectively the underlying and deeper solar spectral features from possible C_3 absorption features on Titan's spectrum, which was a considerable issue at lower resolutions (R. Rianço-Silva et al. 2024).

Hence, despite the significantly deeper solar spectral features, comparison with a set of model spectra of Titan's atmosphere with increasing abundances of C_3 has enabled identifying matching features that deviated away from the R. Kurucz (2006) solar spectrum. We identify 10 absorption features deviating by more than 1σ away from the solar spectrum, and matching the depth and position of C_3 absorption features. Although some of these observed non-solar spectral features may appear to slightly deviate from the predicted C_3 absorption line position, from H. Fan et al. (2024), in all cases the deviation is within this line list errorbar of 0.05 Å (see Table D1).

Despite the compelling case for the detection of C_3 in Titan with the 10 matching absorption features described above, none of the individual potential C_3 features deviates from the $N = 0$ spectrum by 5σ, which would be required to claim a detection just by observing one individual line. This was addressed by performing 2 independent statistical analysis to the model fit to the VLT-ESPRESSO spectrum. The first consisted in calculating the χ^2 curve of the model fit as a function of C_3 column density (following the approach used in C. Nixon et al. 2020). This yielded a strong minimum at $N = 1.5 \times 10^{13}$ cm^{-2} consistent with a C_3 detection at 8σ. The second approach consisted in applying a simple Bayesian MCMC retrieval (I. P. Waldmann et al. 2015) (D. Foreman-Mackey et al. 2013), fitting the spectral model to the observed spectrum. With this approach, it was possible to retrieve the total C_3 column density, N, and temperature, T, that would provide the best model fit to the observed spectrum.

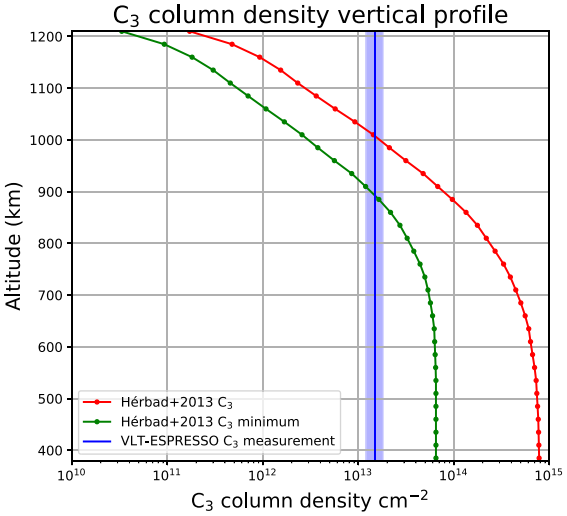

Figure 6. Vertical profile of C_3 column density (from the top of the atmosphere down to the altitude shown in the *y*-axis), obtained from the integration in altitude of the E. Hébrard et al. (2013) predicted vertical profile of C_3, for the median profile obtained from the uncertainty propagation study of C_3 (in red) and for the first 20-quantile distribution (in green, described as C_3 minimum predicted profile). The blue line and errorbar correspond to the C_3 column density retrieved in this work, with the 5σ associated errorbar.

Crucially, this fit has enabled retrieval of a C_3 column density of $N = \left(1.38^{+0.36}_{-0.35}\right) \times 10^{13}$ cm^{-2} (at 5σ), hence ruling out the $N = 0$ scenario (no C_3 on Titan) at 5σ, enabling a detection of C_3 on Titan. In spite of the larger relative errorbars and poorly constrained posterior (which does not show a strong peak), the retrieved temperature value for the C_3 absorbing layer, $T = 422^{+58}_{-171}$ K, is broadly in agreement with the expected temperature in Titan's mesosphere ($T \sim 200$K), where M. Dobrijevic et al. (2016) predict that C_3 is more abundant.

The retrieved value of C_3 column density on Titan's upper atmosphere in this work can be compared to the predicted C_3 abundance profiles from previous modelling studies of Titan's atmospheric chemistry (E. Hébrard et al. 2013; M. Dobrijevic et al. 2016). Taking the predicted vertical profile of C_3 mixing ratio from fig. 4 of E. Hébrard et al. (2013) and integrating it over the multiple altitude layers, using the (N. Teanby et al. 2009) atmospheric density profile, we have obtained the equivalent prediction of column density of C_3 as a function of altitude, down to 400 km of altitude, which is shown in Fig. 6. It is worth mentioning that the (E. Hébrard et al. 2013) vertical abundance profiles are sourced from 900 MCMC runs of the photochemical model, for which a median profile and 20-quantile profiles are obtained. The median predicted C_3 column density down to 400 km of altitude from the (E. Hébrard et al. 2013) photochemical model is of 7.8×10^{14} cm^{-2} (column density vertical profile shown in red), 50 times higher than our C_3 column density measurement with VLT-ESPRESSO. However, for the first 20-quantile of the predicted C_3 distribution (column density vertical profile shown in green), the predicted column density of C_3 down to 400 km is of 6.5×10^{13} cm^{-2}, a value 3 times higher than our VLT-ESPRESSO measurement. The observed discrepancy between our observed value and the lower limit for the (E. Hébrard et al. 2013) photochemical model prediction of a factor or 3 is significantly smaller than the prediction's uncertainty window (the model's median profile compared to the first 20-quantile) which spans over a factor of 12. However, this slight discrepancy but could point towards chemical processes unaccounted for in (E. Hébrard et al. 2013) that could result in a slight C_3 depletion in Titan's upper atmosphere. Updates to Titan's hydrocarbon chemistry have been further explored recently (J. Loison et al. 2019; K. Willacy et al. 2022), but no updated C_3 vertical profiles have been published since (E. Hébrard et al. 2013), hence we suggest future modelling works to explore updates to C_3 photochemistry in Titan.

In order to further constrain the vertical profile of C_3 in Titan's mesosphere and draw direct comparisons between its observed vertical profile with other photochemical species and photochemical model predictions, we suggest using a more thorough radiative transfer model of Titan's atmosphere, with vertical resolution, rather than a simple one-layer model as used in this work. This one-layer model can be thought of as an oversimplification of the line formation, treating it as a 'screen' on the spectrum absorbing only at a fixed altitude. However, in order to accomplish this altitude-dependent spectrum, more information regarding the C_3 electronic transitions is required when compared to the available information for the 4050 Å absorption band (H. Fan et al. 2024) (e.g. the air-broadened line width, and pressure shifts in line position). Nonetheless, the fact that C_3 absorption occurs so high in Titan's atmosphere (above 300 km) in a low-pressure environment causes Doppler-broadening to dominate the line shape, making a Gaussian line profile a reasonable assumption (J. Tennyson et al. 2014). One such complete line list of C_3 was recently published by ExoMol (A. Lynas-Gray et al. 2024) for C_3 mid-infrared transitions for wavelengths longward of 5μm. Hence we recommend further search and modelling efforts of C_3 absorption on Titan on observational data spanning mid-infrared wavelengths, such as those recently published based on *JWST*-MIRI (C. Nixon et al. 2025).

To conclude, we further highlight the great usefulness of instruments originally designed for exoplanet research, such as VLT-ESPRESSO (F. Pepe et al. 2021), or even techniques developed to address the low-SNR nature of exoplanet spectra, such as the Bayesian MCMC likelihood spectral retrievals (I. P. Waldmann et al. 2015), when applied to Solar system targets and science cases. On the advent of a golden era of technical and scientific development aimed at exoplanet research [e.g. with future telescopes and instruments such as Ariel (G. Tinetti et al. 2018) and ELT-ANDES (E. Palle et al. 2025)] it is also worth taking a look back at our own cosmic backyard and revisit many of its mysteries yet to be solved with the light of this new knowledge.

ACKNOWLEDGEMENTS

This work was supported by Fundação para a Ciência e Tecnologia (FCT) of reference PTDC/FIS-AST/29942/2017, through national funds and by FEDER through COMPETE 2020 of reference POCI-01-0145-FEDER-007672, and through the research grants UIDB/04434/2020, UIDP/04434/2020 and UID/04434/2025. RRS acknowledges funding through the FCT fellowship grant 2024.02527.BD. This study was based on observations collected at the European Organisation for Astronomical Research in the Southern Hemisphere under ESO programme 114.277N.

DATA AVAILABILITY

The observational data used in this study are publicly available at the ESO Science Archive, associated with the observing program 114.277N. We further add, as supplementary materials to this

paper, the spectral data used in this study (Titan's spectrum and the model spectra used in this analysis).

REFERENCES

Arney G., Meadows V., Domagal-Goldman S., Deming D., Robinson T., Tovar G., Wolf E., Schwieterman E., 2017, ApJ, 836, 49
Coustenis A. et al. 2010, Icarus, 207, 461
Dekker H., D'Odorico S., Kaufer A., Delabre B., Kotzlowski H., 2000, in Iye M., Moorwood A. F. M., eds, Proc. SPIE Conf. Ser. Vol. 4008, Optical and IR Telescope Instrumentation and Detectors. SPIE, Bellingham
Dias J., Machado P., Ribeiro J., 2022, Atmosphere, 13, 461
Dobrijevic M., Loison J., Hickson K., Gronoff G., 2016, Icarus, 268, 313
Douglas A., 1951, ApJ, 114, 466
Ehrenfreund P., Rasmussen S., Cleaves J., Chen L., 2006, Astrobiology, 6, 3
Fan H. et al., 2024, A&A, 681, A6
Foreman-Mackey D., Hogg D., Lang D., Goodman J., 2013, PASP, 125, 306
Gausset L., Herzberg G., Lagerqvist A., Rosen B., 1965, ApJ, 142, 45
Giorgini J. et al., 1996, BAAS, 28, 1158
Hébrard E., Dobrijevic M., Loison J., Bergeat A., Hickson K., Caralp F., 2013, A&A, 552, A132
Hörst S. M., 2017, J. Geophys. Res., Planets, 122, 432
Kasten F., Young A., 1989, Appl. Opt., 28, 22
Kurucz R., 2006, preprint (arXiv:astro-ph/0605029)
Loison J., Dobrijevic M., Hickson K., 2019, Icarus, 329, 55
Lombardo N. et al., 2019, ApJ, 881, L33
Lorenz R., Lemmon M., Smith P., Lockwood G., 1999, Icarus, 142, 391
Lynas-Gray A., Polyansky O., Tennyson J., Yurchenko S., Zobov N., 2024, MNRAS, 535, 1439
MacKenzie S. et al., 2021, Planet. Sci. J., 2, 112
Machado P., Silva J., Brasil F., Ribeiro J., Gonçalves R., Silva M., 2023, Universe, 9, 491
Mebel A., Agúndez M., Cernicharo J., Kaiser R., 2023, ApJ, 945, L40
Nixon C. et al., 2020, AJ, 160, 205
Nixon C. et al., 2025, Nat. Astron., 9, 969
Palle E. et al., 2025, Exp. Astron., 59, 29
Palmer P. et al., 2001, J.G.R Atmospheres, 106, 14539
Pepe F. et al., 2014, Astron. Nachr., 335, 10
Pepe F. et al., 2021, A&A, 645, A96
Riançо-Silva R., Machado P., Martins Z., Lellouch E., Loison J.-C., Dobrijevic M., Dias J., Ribeiro J., 2024, Planet. Space Sci., 240, 105836
Sánchez-Lavega A., 2010 An Introduction to Planetary Atmospheres (1st ed.), CRC Press, Boca Raton, FL
Savitzky A., Golay M., 1964, Anal. Chem., 36, 8
Schmidt M. R., owski J. K., Galazutdinov G. A., Zhao D., Haddad M. A., Ubachs W., Linnartz H., 2014, MNRAS, 441, 1134
Swings P., McKellar A., Rao K. N., 1953, MNRAS, 113, 571
Tanabashi A., Hirao T., Amano T., Bernath P., 2005, ApJ, 624, 1116
Taylor J. et al., 2023, MNRAS, 524, 817
Teanby N., Irwin P., de Kok R., Jolly A., Bézard B., Nixon C., Calcutt S., 2009, Icarus, 202, 2
Tennyson J. et al., 2014, Pure Appl. Chem., 86, 1931
Tinetti G. et al., 2018, Exp. Astron., 46, 135
Trainer M., Pavlov A., DeWitt H., Jimenez J., McKay C., Toon O., Tolbert M., 2006, Proc. Natl. Acad. Sci., 103, 48
Villanueva G., Smith M., Protopapa S., Faggi S., Mandell A., 2018, J. Quant. Spectrosc. Radiat. Transf., 217, 86
Vuitton V., Yelle R. V., McEwan M., 2007, Icarus, 191, 722
Vuitton V., Yelle R. V., Cui J., 2008, J. Geophys. Res., Planets, 113, E5
Waldmann I. P., Tinetti G., Rocchetto M., Barton E. J., Yurchenko S. N., Tennyson J., 2015, ApJ, 802, 107
Willacy K., Chen S., Adams D., Yung Y.L., 2022, ApJ, 933, 230
Xue Q., Bean J., Zhang M., Welbanks L., Lunine J., August P., 2024, ApJ, 963, L5
Yung Y. L., Allen M., Pinto J., 1984, ApJS, 55, 465

SUPPORTING INFORMATION

Supplementary data are available at *MNRAS* online.

suppl_data

Please note: Oxford University Press is not responsible for the content or functionality of any supporting materials supplied by the authors. Any queries (other than missing material) should be directed to the corresponding author for the article.

APPENDIX A: SPECTRAL DATA REDUCTION

Here we show in detail the steps taken to perform the data reduction of the spectral data obtained from the observations with VLT-ESPRESSO. As mentioned in Section 2, we have obtained seven spectral exposures of Titan, each 20 min long, encompassing a total observation time of 2 h 20 min. Over the course of this time, Titan is observed between airmasses of 1.15 and 1.80, leading to distinct telluric extinctions on the observed spectrum over the course of the night. Fig. A1 shows a comparison between the differing spectra originated on each of the seven exposures, highlighting the distinct continua across exposures taken when Titan was observed at distinct airmasses.

To correct this, each spectral exposure was divided by the spectral exposure with the lowest airmass (the third exposure), and this ratio was fit by a third-degree polynomial across the entire spectrum, as shown in Fig. A2, which zooms in on the same short wavelength range as Fig. A1. Each spectral exposure was then

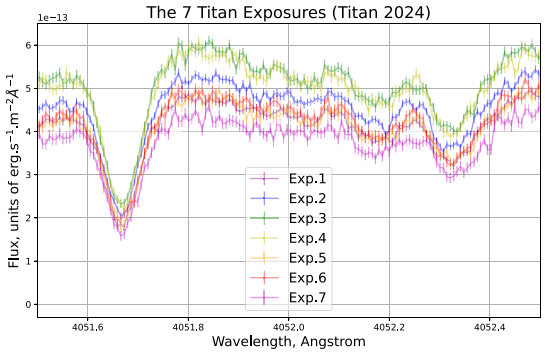

Figure A1. Seven spectral exposures of Titan obtained by VLT-ESPRESSO, each 20 min long (zoomed into a narrow spectral region, for clarity).

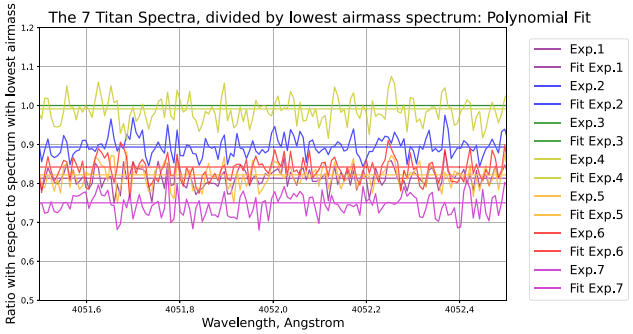

Figure A2. Seven spectral exposures of Titan obtained by VLT-ESPRESSO divided by the spectral exposure observed with the lowest airmass (third exposure), and their respective third-degree polynomial fits (zoomed in the same spectral region as Fig. A1 for clarity).

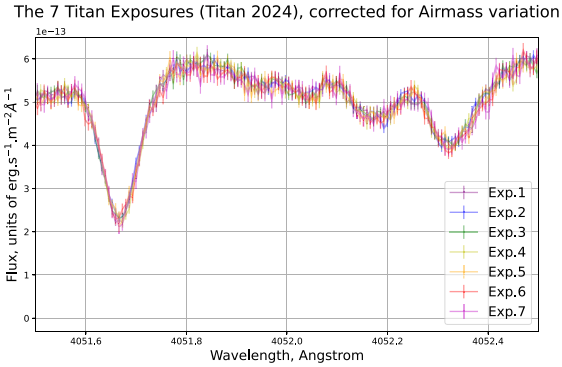

Figure A3. Seven spectral exposures of Titan obtained by VLT-ESPRESSO corrected for different airmass extinctions (zoomed in the same spectral region as Fig. A1 for clarity).

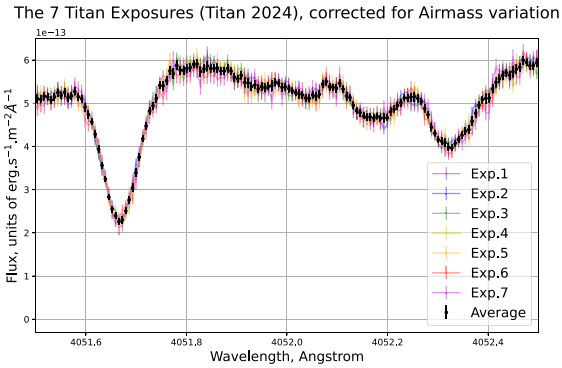

Figure A4. Seven spectral exposures of Titan obtained by VLT-ESPRESSO corrected for different airmass extinctions with spectral average and respective errorbars (zoomed in the same spectral region as Fig. A1 for clarity).

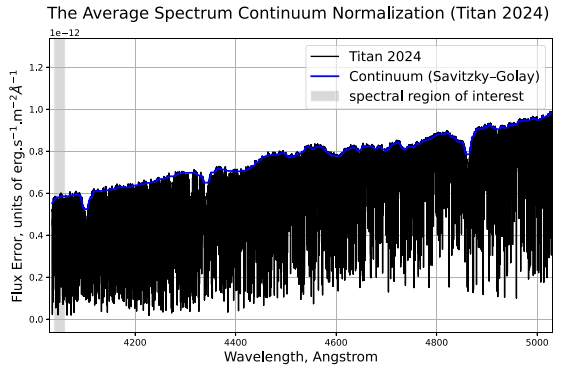

Figure A5. Continuum extraction from the average spectrum of Titan with a Savitzky-Golay filter to enable the normalization of the spectrum – across a larger spectral region, for clarity. The spectral region of interest for this study (4040–4060 Å) is shown in gray.

divided by the polynomial fit to their respective ratio with respect to the exposure with the lowest airmass, allowing to correct the continuum differences across spectral exposures – allowing the distinct spectral exposures to share the same continuum, as shown in Fig. A3.

After sharing a similar spectral continuum, the spectral exposures were averaged into a single spectrum of Titan, with an increased SNR, as shown in black, in Fig. A4. In Fig. A5 we show

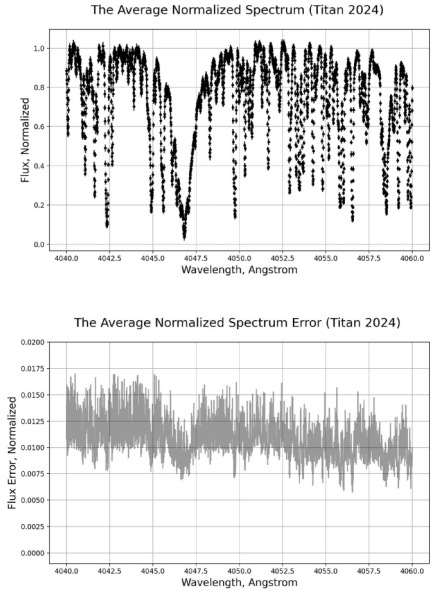

Figure A6. Top: Average normalized spectrum of Titan in the spectral region of interest for the search for C_3 (4040–4060 Å). Bottom: Spectral flux errors of the averaged, normalized spectrum as a function of wavelength in the spectral region of interest for the search of C_3.

the obtention of the spectral continuum using the Savitzky-Golay filter (A. Savitzky & M. Golay 1964) – across a larger spectral region, for clarity – used to normalize the average spectrum of Titan. Finally, in the joint plot of Fig. A6, we show the final averaged and normalized spectrum of Titan on top, in the region of interest for the search for C_3 (4040–4060 Å). At the bottom of Fig. A6 we plot the spectral flux errors of the averaged, normalized spectrum shown at the top of this figure. We observe that despite some modulation that reflects that of the spectral flux (indicating that uncertainties are dominated by photonic error), the spectral error does not vary widely as a function of wavelength on the spectral section used in this study.

APPENDIX B: DERIVATION OF AIRMASS INTEGRATION ON TITAN'S VISIBLE DISC

Here we derive the expression and value of the two-way airmass, integrated across the entirety of Titan's observed disc.

We consider Titan as a fully illuminated sphere, observed as a resolved disc. Let's consider spherical coordinates for Titan. We define the polar angle, θ, as the angle between a given position on Titan's observed sphere and the sub-Earth point on Titan. A surface element of the observed sphere of Titan is given by dS in equation (B1), whereas due to its spherical geometry, the apparent surface element of the sphere projected onto the observed disc is given by $dS_{\rm APP} = \cos(\theta)dS$, or by equation (B2).

$$dS = R^2 \sin(\theta) d\theta d\phi \quad \text{(B1)}$$

$$dS_{\rm APP} = R^2 \sin(\theta)\cos(\theta) d\theta d\phi. \quad \text{(B2)}$$

Considering Titan as a Lambertian reflector – rather than a perfect reflector – we shall include a further $\cos(\theta)$ term on $dS_{\rm APP}$, to account Lambertian scatter, as

$$dS_{\rm APP} = R^2 \sin(\theta)\cos^2(\theta) d\theta d\phi. \quad \text{(B3)}$$

We define 'airmass', $A(\theta)$, as the factor by which the Titan atmospheric pathlength of a straight line (towards Earth) from

a given position on Titan's observed disc is enlarged with respect to the minimum atmospheric pathlength, at the sub-Earth point in Titan, where $A(\theta = 0) = 1$. This airmass is dependent on the polar angle θ on Titan's sphere, and is given by equation (B4) following the plane-parallel atmosphere approximation.

$$A(\theta) = \frac{1}{\cos(\theta)}. \tag{B4}$$

We wish to calculate the integrated airmass $< A >$ over the disc of Titan observed by us. This requires an integration of airmass $A(\theta)$ over the whole of the observed apparent disc of Titan. Considering we observed Titan centred on its apparent disc's centre, we shall integrate over the polar angle between the centre of the disc, $\theta = 0$, up until the maximum observed polar angle, $\theta = \alpha$, which is defined by the relative size of VLT-ESPRESSO's fiber (0.5 arcsec) with respect to Titan's apparent size (0.826 arcsec), on the night of the observation, as

$$\alpha = \arcsin\left(\frac{0''.5}{0''.826}\right) \approx 37.25^{\circ}. \tag{B5}$$

Hence, the integration of $A(\theta)$ over the apparent observed disc of Titan (normalized by the integrated element of apparent surface area) is given by

$$< A >= \frac{\iint A(\theta) dS_{\rm APP}}{\iint dS_{\rm APP}} = \frac{\int_0^{2\pi} d\phi \int_0^{\alpha} A(\theta) R^2 \cos^2(\theta)\sin(\theta) d\theta}{\int_0^{2\pi} d\phi \int_0^{\alpha} R^2 \cos^2(\theta)\sin(\theta) d\theta}. \tag{B6}$$

Replacing $A(\theta)$ by equation (B4), we get

$$< A >= \frac{\int_0^{\alpha} \cos(\theta)\sin(\theta) d\theta}{\int_0^{\alpha} \cos^2(\theta)\sin(\theta) d\theta} = \frac{3}{2} \cdot \frac{1 - \cos^2(\alpha)}{1 - \cos^3(\alpha)}. \tag{B7}$$

We must consider a two-way airmass for Titan, given that the radiation interacts twice with the column of C_3 absorbing gas: when it arrives to Titan, descending all the way to Titan's optical radius, and after being backscattered upwards, close to Titan's optical radius at altitudes of 300 km (for 400 nm photons), on its way out of Titan's atmosphere. Hence the integrated two-way airmass on the observed disc of Titan, $\tilde{A}$, is given by equation (B8).

$$\tilde{A} = 3 \cdot \frac{1 - \cos^2(\alpha)}{1 - \cos^3(\alpha)}. \tag{B8}$$

If we had observed the entirety of Titan's disc, $\alpha = \pi/2$, which would yield an integrated two-way airmass of 3. However, the incomplete coverage of Titan's disc by the VLT-ESPRESSO fibre prevents a stronger contribution to the airmass from Titan's limb. This yields, for α given by equation (B5), an integrated two-way airmass on Titan of $\tilde{A} \simeq 2.2155$, for this observation.

To assess whether this plane-parallel atmosphere approximation is valid in the case of such an extended atmosphere as Titan's, we check how different the maximum observed polar angle, α', would be in a spherical atmosphere at the altitude at the peak of C_3 absorption (expected to occur below altitudes of 500 km; M. Dobrijevic et al. 2016; R. Rianço-Silva et al. 2024), when the plane-parallel α was obtained for the optical radius altitude (300 km). This corrected maximum observed polar angle α' is obtained by equation (B9):

$$\alpha' = \arccos\left[\sqrt{1 - \left(\frac{R}{R+H}\sin(\alpha)\right)^2}\right] \tag{B9}$$

with R as the optical radius of Titan (equal to the solid body of Titan + 300 km at $\lambda = 400$ nm; R. Lorenz et al. 1999) and H as the altitude of the layer of interest above R (i.e. the expected altitude of maximum C_3 absorption at 500 km, and hence $H = 200$ km above the optical radius of Titan), and α as the maximum observed polar angle at the optical radius, given by equation (B5). Using this, we retrieve $\alpha' = 34.36^{\rm o}$. Applying this new angle to the integrated airmass formula (equation B8), we get $\tilde{A}' = 2.1845$ which compares to the $\tilde{A} = 2.2155$ integrated airmass obtained from the plane-parallel approximation, deviating by less than 1.5 per cent with respect to one another.

One other example of the effect of spherical geometry on an atmosphere which is not accounted by the plane-parallel approximation is the correct expression for the airmass at a given zenithal angle. The plane-parallel atmosphere approximation describes airmass by equation (B4), which diverges for $\theta = 90^{\rm deg}$. A commonly used spherical correction for this effect is given in (F. Kasten & A. Young 1989). Using their formulation, we numerically integrated this airmass over an apparent planetary disc, up to a maximum angle α. We noticed that for maximum integration angles (maximum observed polar angles) below $40^{\rm o}$, the plane-parallel and the spherical geometry formulation of (F. Kasten & A. Young 1989) do not differ by more than 0.1 per cent. Taking this into account, we conclude that the plane-parallel approximation provides a maximum deviation from spherical geometry integrated airmass 'true' value of less than 1.5 per cent, and hence constitutes a valid approximation for this observation, when only the central regions of Titan's apparent disc are probed.

APPENDIX C: SPECTRAL RESIDUALS

We display here the residual plots resulting from the fit of two spectral models, one without C_3 and another corresponding to the MCMC best fit to the data, with respect to the VLT-ESPRESSO data of Titan. This is a direct comparison with Fig. 5 where spectral models are compared to the observed spectrum. In these residuals, we subtract the models to the observed spectrum, assessing how different are the residuals for the no-C_3 case with respect to the MCMC retrieval best-fitting model which requires the presence of C_3 as described in Section 4.3. The shaded grey area corresponds to the region where residuals are smaller than the observed spectrum's uncertainty, which means that the model agrees with the observation in those wavelengths.

As expected, we observe that the spectral regions where the two residuals differ align with the C_3 modelled spectral lines. Interestingly, in these regions, the residual of the MCMC best-fitting model (with C_3) is overall closer or within the shaded region that corresponds to the observations – i.e. as shown above with the χ^2 analysis and the MCMC fit, the spectral model containing C_3 provides a better fit to the observed spectrum of Titan than the spectral model without C_3.

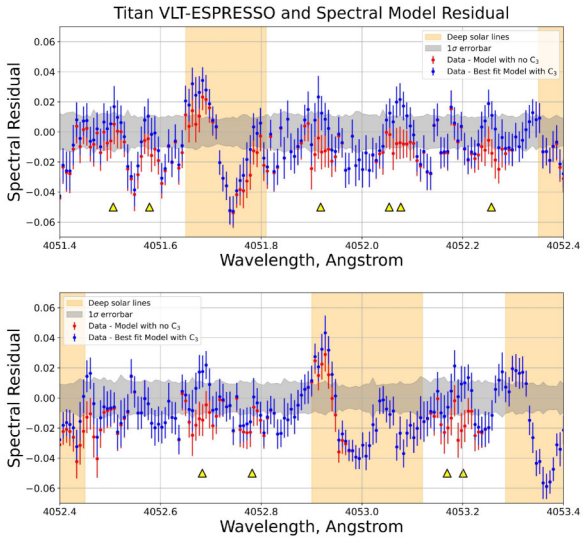

Figure C1. Residual plots of two distinct spectral models with respect to VLT-ESPRESSO spectrum of Titan. This figure directly compares with Fig. 5, where in red we showcase the residuals resulting from the subtraction of no-C_3 spectral model to the observed spectrum of Titan, and in blue we showcase the residuals resulting from the subtraction of the MCMC best-fitting model (with C_3) to the observed spectrum of Titan. The shaded grey area corresponds to the region around residuals $= 0$ smaller than the Titan's observed spectrum 1σ errorbars – i.e. region of model agreement with observation within its uncertainty. The shaded orange region corresponds to spectral regions dominated by deep solar absorption lines (> 30 per cent of relative depth). Triangle markers show the central wavelength of the C_3 spectral lines according to (H. Fan et al. 2024).

APPENDIX D: C_3 LINE LIST AND LINE DETECTION

We display here Table D1 containing the line list of C_3 used to model the absorption spectrum of C_3 in this work. It also includes the detected line wavelengths, line depth with respect to the solar spectrum and detection significance (ratio between line depth and VLT-ESPRESSO errorbars at line centre).

Table D1. Line list for the C_3 $\tilde{A} - \tilde{X}$ 000–000 band based in H. Fan et al. (2024), showcasing each identified transition (P(J), Q(J), R(J)), original wavelength, λ_j, in Å, oscillator strength, f_j, and the observed matching features in wavelength, λ, observed relative line depth and detection line significance (scaled by the data flux errorbars at the detected line). 'O.D.S.L.' at the 'observed line' column stands for 'Overlapping with a Deep Solar Line', meaning that the expected C_3 absorption feature was overlapped with a deep solar absorption feature (solar line depth > 10 per cent), preventing its identification. ** refers to C_3 lines which may be merged with other close C_3 lines, making individual detections challenging. The last column showcases the shifts applied to the original line list for the adapted line list test performed in Appendix E.

Rotational line	Original λ_j, Å	f_j (x10^3)	Observed line λ_j, Å	Observed line depth (%)	Line detection significance	Adapted line list, line shift $\Delta\lambda_j$, Å
R(20)	4049.808	4.29	O.D.S.L.	-	-	-
R(18)	4049.861	4.32	O.D.S.L.	-	-	-
R(16)	4049.962	4.36	O.D.S.L.	-	-	-
R(14)	4050.075	3.49	O.D.S.L.	-	-	-
R(12)	4050.191	3.58	O.D.S.L.	-	-	-
R(10)	4050.327	3.73	O.D.S.L.	-	-	-
R(6)*	4050.401	0.58	O.D.S.L.	-	-	-
R(8)	4050.484	3.95	O.D.S.L.	-	-	-
R(4)*	4050.567	0.49	O.D.S.L.	-	-	-
R(6)	4050.661	4.21	O.D.S.L.	-	-	-
Q(2)*	4050.746	0.45	O.D.S.L.	-	-	-
R(4)	4050.857	4.44	O.D.S.L.	-	-	-
R(2)	4051.055	3.78	O.D.S.L.	-	-	-
R(2)*	4051.190	2.08	O.D.S.L.	-	-	-
R(0)	4051.255	4.22	O.D.S.L.	-	-	-
R(0)*	4051.396	10.58	O.D.S.L.	-	-	-
Q(2)	4051.448	6.87	O.D.S.L.	-	-	-
Q(4)	4051.506	7.70	4051.54	4.3	3.2σ	+0.04
Q(6)	4051.578	7.89	4051.60	3.1	2.6σ	+0.03
Q(8)	4051.670	7.95	O.D.S.L.	-	-	-
Q(10)	4051.782	7.96	O.D.S.L.	-	-	-
P(2)	4051.820	1.06	O.D.S.L.	-	-	-
Q(12)	4051.918	7.97	4051.90	2.7	2.1σ	−0.01
P(4)	4052.054	1.57	4052.02	2.4	2.2σ	−0.03
Q(14)	4052.077	7.98	4052.11**	2.0	2.4σ	+0.04
Q(6)*	4052.122	0.28	No match**	-	-	-
P(4)*	4052.180	0.86	No match**	-	-	-
Q(16)	4052.257	7.98	4052.27	1.9	1.6σ	+0.01
P(6)	4052.412	2.56	O.D.S.L.	-	-	-
Q(18)	4052.459	7.99	O.D.S.L.	-	-	-
P(8)*	4052.521	0.39	O.D.S.L.	-	-	-
Q(20)	4052.683	7.99	4052.67	3.2	2.2σ	−0.01
P(8)	4052.782	2.82	4052.77	2.3	2.4σ	-
Q(22)	4052.938	7.99	O.D.S.L.	-	-	-
P(10)	4053.169	2.87	4053.15	2.3	1.8σ	-
Q(24)	4053.201	7.99	4053.19	3.5	2.7σ	-
Q(26)	4053.479	7.99	O.D.S.L.	-	-	-
P(12)	4053.577	2.87	O.D.S.L.	-	-	-
Q(28)	4053.783	8.00	O.D.S.L.	-	-	-
P(14)	4054.005	2.86	O.D.S.L.	-	-	-
Q(30)	4054.108	8.00	O.D.S.L.	-	-	-
P(16)	4054.447	3.64	O.D.S.L.	-	-	-
P(18)	4054.902	3.68	O.D.S.L.	-	-	-
P(20)	4055.369	3.71	O.D.S.L.	-	-	-

APPENDIX E: ADAPTED C_3 LINE LIST AND RETRIEVAL

MCMC retrievals provide an interesting way to compare between distinct model fits to the same data set (I. P. Waldmann et al. 2015). After noticing a slight mismatch between some identified spectral features on the VLT-ESPRESSO spectrum of Titan and the expected C_3 line positions, we suggested these mismatches could be due to the empirical nature of the (H. Fan et al. 2024) line list, which was obtained at a worse spectral resolution than these VLT-ESPRESSO observations. Hence, in Table D1 we suggest small shifts (below the (H. Fan et al. 2024) typical line wavelength uncertainty of 0.05 Å) that could be expected to improve the overall fit to the data. This was tested by applying the same MCMC retrieval test described in Section 4.3, comparing the posteriors obtained by using the original (H. Fan et al. 2024) versus the adapted line lists – as shown in Fig. E1, with the best-fitting plot shown in Fig. E2 and the residual plots in Fig. E3.

As expected, the adapted line lists corner plot and histograms show a better temperature constraint (in blue, following a dis-

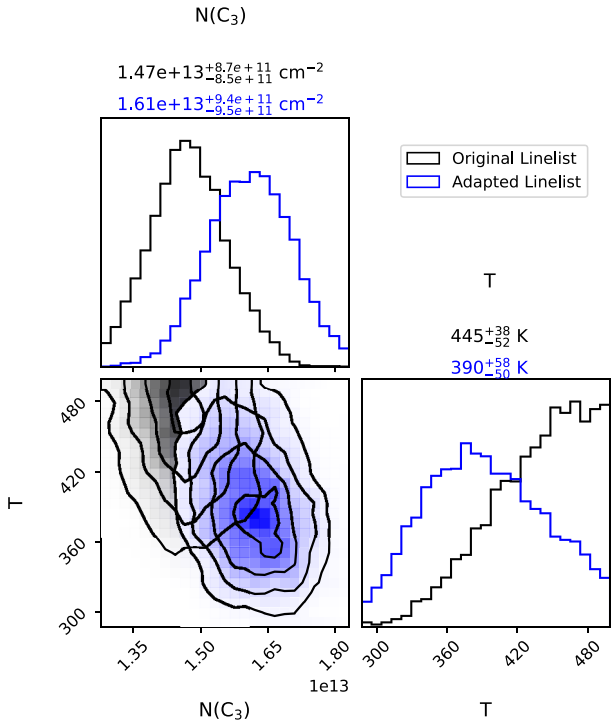

Figure E1. Posterior plots from the MCMC fit to the VLT-ESPRESSO spectrum of Titan – for the original (H. Fan et al. 2024) C_3 (black) and our suggested adapted line list, which improves the spectral model match to the observed spectral features (blue). Fit for the column density of C_3 (N) and for the temperature (T). Retrieved values showcased with 1σ errorbars. Contour plots on the 2D histogram correspond to the 0.5σ, 1σ, 1.5σ, and 2σ confidence regions for a 2D Gaussian distribution.

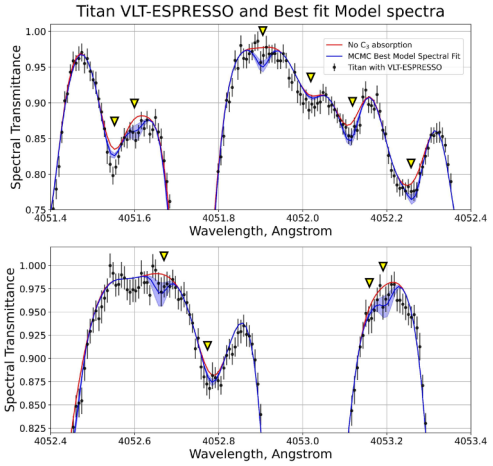

Figure E2. VLT-ESPRESSO normalized spectrum of Titan (black data points) at the spectral region of interest for the $\tilde{A}^1\Pi_u - \tilde{X}^1\Sigma_g^+$ 000–000 band of C_3 compared to the backscattered solar spectrum (a proxy for Titan's spectrum with no C_3 absorption, in red) and to the best-fitting model obtained from the MCMC likelihood fit with the adapted C_3 line list described in Table D1, associated with the retrieved values for $N(C_3)$ and T, in blue. The shaded blue area corresponds to the best-fitting model uncertainty based on the retrieved $N(C_3)$ and T values with 3σ errorbars. The triangles mark the identified spectral features we associate with C_3 absorption features, described in Table D1.

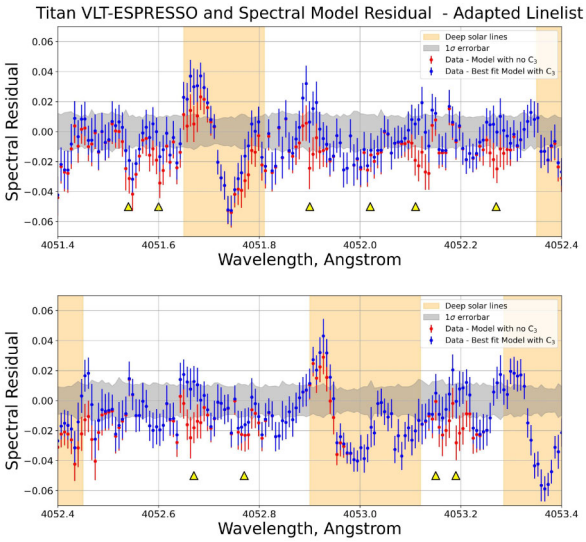

Figure E3. Residual plots of two distinct spectral models with respect to VLT-ESPRESSO spectrum of Titan. This figure directly compares with Fig. C1, albeit with the adapted C_3 line list, rather than the original line list by (H. Fan et al. 2024). In red we showcase the residuals resulting from the subtraction of no-C_3 spectral model to the observed spectrum of Titan, and in blue we showcase the residuals resulting from the subtraction of the MCMC best-fitting model (with C_3) to the observed spectrum of Titan. The shaded grey area corresponds to the region around residuals $= 0$ smaller than the Titan's observed spectrum 1σ errorbars – i.e. region of model agreement with observation within its uncertainty. The shaded orange region corresponds to spectral regions dominated by deep solar absorption lines (> 30 per cent of relative depth). Triangle markers show the central wavelength of the C_3 spectral lines according to our adapted line list.

tribution closer to a Gaussian curve within the allowed prior range) than the original line list (black). The retrieved C_3 abundance using the adapted line list is shown (from its marginalized histogram) to be slightly higher for the original line list, at $N(C_3)$, with $N(C_3) = (1.61 \pm 0.09) \times 10^{13}$ cm^{-2} at 1σ, $N(C_3) = \left(1.61^{+0.29}_{-0.28}\right) \times 10^{13}$ cm^{-2} at 3σ and $N(C_3) = \left(1.61^{+0.34}_{-0.36}\right) \times 10^{13}$ cm^{-2} at 5σ– still within the expected errorbars obtained with the original line list. Retrieved temperature values are nonetheless different, due to the better constraint this alternative line list enabled: $T = (390^{+58}_{-50})K$ at 1σ, $T = (390^{+110}_{-126})K$ at 3σ, and $T = (390^{+110}_{-157})K$ at 5σ. A possible explanation is that due to the enhanced fit the spectrum obtained with the adapted line list, the retrieval is not as skewed towards higher temperatures, which tend to improve this fit by broadening the modelled spectrum, bringing them closer to the slightly shifted spectral features in the data.

After confirming the detection of C_3 in Titan's atmosphere through the χ^2 method (Section 4.2) combined with an MCMC retrieval using the original (H. Fan et al. 2024) line list, the retrieval comparison shown could indicate that the adapted line list may indeed be preferred when modelling the 405-nm band of C_3 at ultra-high resolutions.

This paper has been typeset from a TEX/LATEX file prepared by the author.